BNL-212227-2019-JAAM

Isolating the Roles of Hydrogen Exposure and Trace Carbon Contamination on the Formation of Active Catalyst Populations for Carbon Nanotube Growth

J. Carpena-Núñez, J. A. Boscoboinik

To be published in "ACS NANO"

July 2019

Center for Functional Nanomaterials

Brookhaven National Laboratory

U.S. Department of Energy

USDOE Office of Science (SC), Basic Energy Sciences (BES) (SC-22)

DISCLAIMER

Isolating the Roles of Hydrogen Exposure and Trace Carbon Contamination on the Formation of Active Catalyst Populations for Carbon Nanotube Growth

Jennifer Carpena-Núñez,[1,2,] Jorge Anibal Boscoboinik,[2] Sammy Saber,[1] Rahul Rao,[1,3] Jian-Qiang Zhong,[2] Matthew R. Maschmann,[4] Piran R. Kidambi,[5] Nicholas T. Dee,[6] Dmitri N. Zakharov,[2] A. John Hart,[6] Eric A. Stach,[2,7] and Benji Maruyama,[1,†]*

[1] Materials and Manufacturing Directorate, Air Force Research Laboratory, Wright-Patterson Air Force Base, Dayton, Ohio 45433, USA

[2] Center for Functional Nanomaterials, Brookhaven National Laboratory, Upton, NY 11973, USA

[3] UES, Inc., Dayton, Ohio 45431

[4] Department of Mechanical and Aerospace Engineering, University of Missouri, Columbia, MO 65211

[5] Department of Chemical and Biomolecular Engineering, Vanderbilt University, Nashville, TN 37212

[6] Department of Mechanical Engineering, Massachusetts Institute of Technology, Cambridge, MA, 02139

[7] Department of Materials Science and Engineering, University of Pennsylvania, Philadelphia, PA 19104

[*,†] Corresponding author

ABSTRACT

Limited understanding of the factors influencing the yield of carbon nanotubes (CNTs) relative to the number of catalyst particles remains an important barrier to their large-scale production with high quality, and to tailoring CNT properties for applications. This lack of understanding is evident in the frequent use of Edisonian approaches to give high-yield CNT growth, and in the sometimes-confusing influence of trace residues on the reactor walls. In order to create conditions wherein CNT yield is reproducible and to enable large-scale and reliable CNT synthesis, it is imperative to understand –fundamentally– how these common practices impact catalytic activity and thus CNT number density. Herein, we use ambient pressure-X-ray photoelectron spectroscopy (AP-XPS) to reveal the influence of carbon and hydrogen on the coupling between catalyst reduction and CNT nucleation, from an iron catalyst film. We observe a positive correlation between the degree of catalyst reduction and the density of vertically aligned CNTs (forests), verifying that effective catalyst reduction is critical to CNT nucleation and to the resulting CNT growth yield. We demonstrate that the extent of catalyst reduction is the reason for low CNT number density and for lack of self-organization, lift-off, and growth of CNT forests. We also show that hydrocarbon by-products from consecutive growths can facilitate catalyst reduction and increase CNT number density significantly. These findings suggest that common practices used in the field –such as reactor preconditioning– aid in the reduction of the catalyst population, thus improving CNT number density and enabling the growth of dense forests. Our results also motivate future work using AP-XPS and complementary metrology tools to optimize CNT growth conditions according to the catalyst chemical state.

KEYWORDS: carbon nanotubes, nucleation success rate, CNT number density, iron oxide, ambient pressure XPS

Carbon nanotubes (CNTs) possess physical and chemical properties which make them attractive –in various configurations– for use as biological and molecular sensors, energy storage and composite materials, and electrical wires, among other applications.[1-10] The widespread deployment of CNTs, however, still remains hindered by the inability to reproducibly grow high quality CNTs in bulk quantities with selective physical properties (*i.e.* growth of conducting or semiconducting single-wall CNTs with single chirality). In addition, catalyst nucleation success rate in bulk growth –such as the floating catalyst approach– is very low, greatly limiting scale up and increasing the cost of CNTs. Poor and unpredictable growth behaviors emphasize the need for generalities to predict nucleation success rate. In order to increase CNT number density, it is imperative to understand why some catalysts grow tubes and others do not. This is not a trivial task considering the small time scales associated with CNT nucleation and growth, and the large parameter space.

Over the last decade, many studies have established *in situ* experimental platforms to be used as diagnostic tools during CNT growth.[11-30] Environmental transmission electron microscopy (ETEM) and *in situ* Raman spectroscopy have provided crucial mechanistic knowledge regarding catalyst evolution (Ostwald ripening and coalescence), catalyst-support interactions, step flow and cap formation, growth yield, and catalyst lifetime.[20-23, 26] Meanwhile, *in situ* glancing incidence small angle X-ray scattering (GISAXS) has elucidated attributes that influence CNT forest growth, such as catalyst particle size, CNT diameter distribution, and CNT alignment.[11-12, 25-29] Ambient pressure-X-ray photoelectron spectroscopy (AP-XPS), on the other hand, has been used under practical growth conditions to reveal the chemical state of the catalyst during annealing, and to monitor the evolution of carbon at the onset of growth.[11-18, 31] Contradictory findings obtained using this technique, however, stress how the active chemical state of the catalyst remains in debate. For instance, de los Arcos *et al*. claimed that a more oxidized Fe film led to an increase in CNT growth yield,[12] and that catalyst chemical state –the determining factor for growth– is not influenced by the catalyst support chemistry. Meanwhile, Hoffman *et al*. reported fully reduced iron as the active catalytic state[14, 16] and demonstrated that the interaction strength between

the catalyst and support determines the extent of reduction of the catalyst film. They also showed that a catalysts supported on silica, SiO_2, can grow poorly despite being fully reduced due to other influential factors, such as Ostwald ripening.[14, 18, 31-35] The fact that iron catalysts generally result in a higher CNT growth yield when supported on alumina (Al_2O_3) as a result of the strong catalyst-support interaction, which in turn promotes the coexistence of the reduced and oxide phase,[13] raises the question as to whether a partially oxidized catalyst population is needed. Poor CNT yields from fully reduced catalysts (which lead to sparse, non-aligned CNT growth on substrates or low productivity in a floating catalyst approach) emphasize the importance of understanding how the catalyst chemical state affects nucleation success rate. Common practices used to improve growth yield, which may involve using oxidizing agents (*i.e.* oxygen or water) and conducting reactor or catalyst preconditioning procedures (*i.e.* carbonization or 'dummy' growths), suggest that other attributes complementary to the traditional reducing agent (*i.e.* hydrogen) influence nucleation success rate.

In this study, we show that catalyst reduction is indeed the determining factor of nucleation success rate from iron nanoparticles and hence of CNT number density. Using AP-XPS to probe the transformation of iron nanoparticles supported on Al_2O_3, we show how the chemical state of the particle ensemble can determine the growth outcome. We unequivocally demonstrate the importance of achieving a global catalyst reduction for increased growth yield, and show that the partial or minimal reduction of the catalyst film is responsible for poor growth yields. We also examine how reactor preconditioning or sequential experimentation can improve growth by providing hydrocarbon species which reduce the catalyst film more efficiently than hydrogen. We propose that –despite the catalyst type, support type, or experimental conditions involved– nucleation success rate is dictated by catalyst reduction; the choice of catalyst, support, and experimental parameters provides a mixture of conditions that influence the onset and kinetics of reduction and counteract catalyst evolution.

RESULTS AND DISCUSSION

Experimental Procedure. The AP-XPS setup (**Figure S1**) at the National Synchrotron Light Source II (NSLS II, 23-ID-2 beamline) was used to grow high-density, vertically aligned arrays (forests) of predominantly single- and double-wall CNTs (**Figure 1**). Forests were grown in the AP-XPS using standard CVD recipes, with mixtures of oxygen, hydrogen, water vapor, and a hydrocarbon, and catalyst-coated substrates which were mounted onto a heating element. A 1nm iron (Fe) catalyst film was deposited on top of a catalyst support, either by *in situ* or *ex situ* deposition. The catalyst support consisted of a silicon wafer substrate containing a 10nm layer of Al_2O_3 deposited by ALD over a 2-3 nm layer of native silicon dioxide.

In a typical experiment the substrate was introduced to the AP-XPS chamber and heated in 100mTorr of oxygen (O_2) at a temperature of 400°C for 20 min. Oxygen annealing was done to remove excess carbon contaminants (adventitious carbon) on the surface of *ex situ* deposited catalyst films. After oxygen annealing, the chamber was evacuated and the sample cooled down to room temperature. The catalyst film was then exposed to reducing conditions, followed by the CNT growth conditions. Catalyst reduction and particle formation was performed by exposing the catalyst films to 40mTorr of hydrogen (H_2) and increasing the temperature to 750°C, at which point 10mTorr of acetylene (C_2H_2) was introduced in the growth chamber and held for 10 min. Water vapor was used in some experiments to enhance growth; it was introduced in the AP-XPS chamber prior to the hydrogen reduction step. **Figures 1** and **S2** show a schematic representation of the experimental procedure. XPS collection took place throughout the oxidation, reduction, and growth stages of the experiment, as shown in **Figure 1g**. The collected spectra (**Figure 1g**) are discussed later. See the methods section for a more detailed description of sample preparation and experimental procedures.

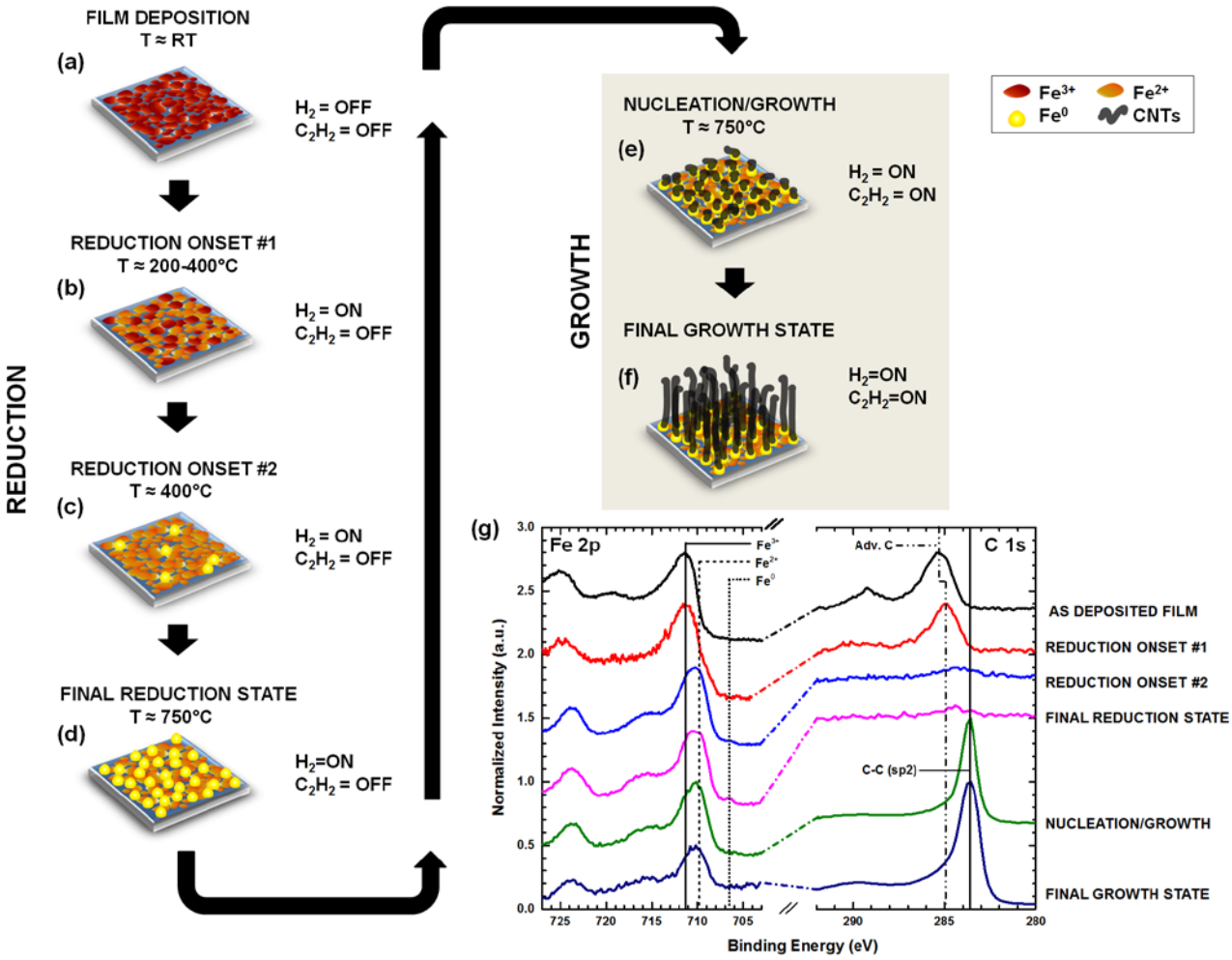

Figure 1. Experimental procedure and exemplary data collected along each stage of the experiment. (a-d) Schematic representation of the reduction of iron catalyst films and particle formation. (e-f) Schematic representation of CNT growth on the population of reduced catalyst particles. (g) AP-XPS spectra for the Fe 2p and C 1s core level spectra at multiple stages of the experiment described in the schematic. The reduction onsets 1 and 2 mark the conversion of the oxide film to a more reduced state, as indicated by the chemical states in the Fe 2p core level spectra (Fe^{3+}, Fe^{2+}, and Fe^{0}).

In order to elucidate the key factors influencing nucleation success rate of catalyst nanoparticles, we studied five samples (labeled **i-v**) with experimental conditions summarized in **Table 1**. Exemplary data collected from

sample **i** are shown in **Figure 1g**. The set included four samples with *ex situ* deposited catalyst (samples **i-iv**), which were exposed to water vapor, hydrogen, and hydrocarbon, and one sample with *in situ* deposited catalyst, which was exposed only to the hydrocarbon (sample **v**). Samples **ii-iv** were grown in succession using increasing amount of water vapor (referred to as 1st Run in **Table 1**); these exhibited a progressive buildup of hydrocarbon by-products, which we refer to as carbon contaminants. The hydrocarbon by-products deposited on the surface of the samples when water reacted with gaseous carbon in the chamber to form solid carbon. Samples **v** and **i** were processed consecutively during a second set of experiments using a clean reactor (referred to as 2nd Run in **Table 1**); therefore, these were not exposed to any oxidants (*i.e.* oxygen or water) prior to reduction and growth. These two samples exhibited relatively clean surfaces, with minimal hydrocarbon by-products present as will be discussed later. Note that samples **i** and **iv** were exposed to equivalent reduction and growth conditions, but that sample **i** had a clean surface while sample **iv** had a highly contaminated surface due to the processing history of the chamber and heating element since cleaning. The surface cleanliness, along with the water vapor pressures used in each run and other growth conditions, are listed in **Tables 1** and **S1**. Although the base pressure of water vapor was deliberately varied from 10^{-8} to 10^{-2} Torr, we observed that this difference had a small impact on growth (see samples **i** and **iv** which were grown using equivalent water vapor pressures) and found that carbon contaminants play a more influential role in reducing the catalyst in a highly oxidizing environment. Hence, the roles of water vapor –an oxidizing agent commonly used to keep the catalyst clean and counteract Ostwald ripening–[9, 36] and of oxygen –an oxidizing agent which can either counteract or enhance Ostwald ripening depending on growth conditions–[37-38] are not addressed in this study. Instead, we focus mainly on the role of carbon contaminants and assess the relevance of these gases during growth in terms of aiding and quenching of reduction of the catalyst.

Table 1. Sample condition summary.

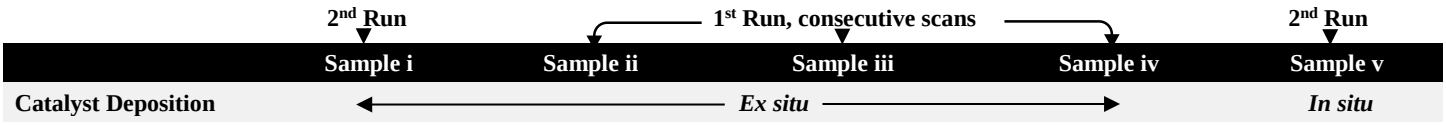

Surface Cleanliness	Clean	Lightly preloaded	Mildly preloaded	Highly preloaded	Clean
Pre-growth anneal in O_2		✓	✓	✓	
Water level	10^{-2} Torr	10^{-6} Torr	10^{-4} Torr	10^{-2} Torr	10^{-8} Torr
Anneal in H_2	✓	✓	✓	✓	

Equivalent reducing and growth conditions in samples i & iv

For the samples listed in **Table 1**, we observed a fluctuation in the nucleation success rate, evidenced by the CNT packing density in scanning electron microscopy (SEM) images of the grown forests (**Figure 2a-j**). Although the samples were not synthesized in chronological order, for clarity we labeled them in order of apparent forest growth quality (determined by visual inspection of the forest density and CNT alignment) and catalyst chemical state (determined from AP-XPS data). CNT growth, conducted using Al_2O_3-supported iron films and standard CVD growth conditions, led to both poor growth (low density, non-aligned, spaghetti-like networks of CNT bundles) and good growth (high-density, vertically-aligned CNT forests). The difference in growth density is –as we discuss later– a direct result of nucleation success rate, which is determined by the catalyst chemical state.

CNT Density and Alignment Dependence on Fe^0/Fe^{2+} Ratio. We found a positive correlation between the degree of reduction of the catalyst film (**Figure 2k-o**) and the CNT alignment within the forests (**Figure 3**). The CNT alignment and apparent density obtained from SEM micrographs (**Figure 2f-j**, explained further below) suggest that the number density of CNTs increases with the amount of the catalyst film that is fully reduced, and that the degree of reduction influences the number density of CNT-bearing catalysts.[32] This degree of reduction was determined for each sample by fitting the corresponding AP-XPS spectrum to obtain the ratio between the zero-valent (Fe^0) and the divalent (Fe^{2+}) states in the Fe $2p_{3/2}$ core level peaks, centered at 706.8 eV and 709.8 eV, respectively. Each spectrum was fit at the onset of nucleation, just before the introduction of the hydrocarbon precursor, using asymmetric and symmetric line shapes (for main peaks and shake-up peaks) and Shirley background subtraction (see Methods for details) as reported elsewhere.[39-45]

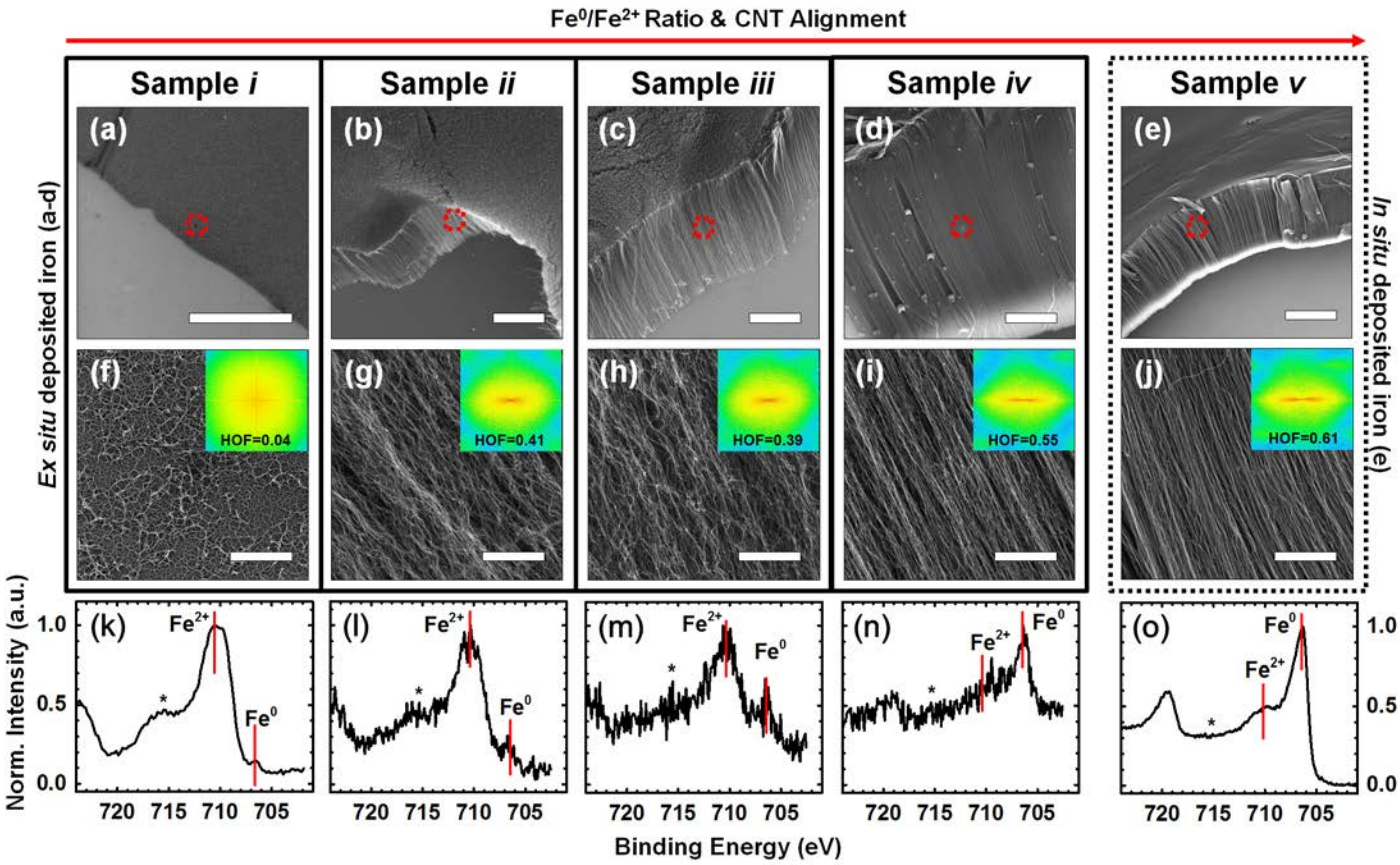

Figure 2. CNT density and alignment are correlated to degree of catalyst reduction. (a-e) SEM micrographs of CNTs grown in the AP-XPS system show the influence of processing parameters on forest alignment and density. (f-j) Corresponding high-magnification micrographs of the areas highlighted by dotted red squares in (a-e). Insets in the bottom panels of (f-j) show the Fast Fourier Transforms and calculated Herman Orientation Factors (HOF) for each SEM micrograph. (k-o) Fe 2p AP-XPS spectra corresponding to panels a-e, respectively. The Fe^{2+} and Fe^{0} chemical states are identified in each sample. The asterisk in (k-o) depicts the shake-up peak of the Fe^{2+} peak, which helps identify the catalyst chemical state. Fe 2p spectra from samples **i-v** show an increase in catalyst reduction (Fe^{0}). Poor growth (a & f) was evident in samples with a small degree of catalyst reduction (k). An increase in apparent forest density with increase in catalyst reduction to Fe^{0} clearly marks the importance of reaching a majority population of catalyst particles in the fully reduced state to achieve good growth. The difference in noise level in between (l-n) and (k & o) is a result of improved signal collection efficiency after

service maintenance of the energy analyzer, which occurred between the 1st and 2nd runs in **Table 1**. The scale bar corresponds to 20μm and 1μm in (a-e) and (f-j), respectively.

To understand how the catalyst chemical state determines growth density, we use the Herman Orientation Factor (HOF) as a quantitative metric; the HOF is calculated from the fast Fourier transform (FFT) of each SEM micrograph (shown in the insets in **Figures 2f-j** and described in detail in the Methods section). An increase in the calculated HOF values, up to a factor of ~10, was observed with increase in Fe^0 content (**Figure 3**, black squares). Meanwhile, the forest height (**Figure 3**, blue circles) increased linearly for all samples except sample **v** (*in situ* deposited catalyst), reaching a height of up to ~100μm. Sample **v** grew a forest of intermediate height (~27μm), taller than samples **i** and **ii**, but shorter than samples **iii** and **iv**. The difference in forest height between samples **iv** and **v**, the two samples with highest Fe^0 content, will be discussed in the following segment. We note that aside from sample **i**, all the other samples (**ii-v**) produced high-density, vertically aligned CNT forests. And, although the metric used herein to define good growth is CNT alignment (not CNT density), GISAXS and TEM studies have revealed that CNT alignment and number density are directly correlated,[27] thus validated the calculated HOF values as an indirect measurement of CNT number density. This density-alignment correlation is also validated by visual inspection of the SEM micrographs. A proportional increase in the HOF with Fe^0/Fe^{2+} ratio (**Figure 3**) indicates that there is a direct relationship between the amount of fully reduced iron (in the Fe^0 state) and the density-alignment of the forests. This is especially evident in sample **i**, which exhibited the lowest content of Fe^0 and hence the least alignment and density (**Figures 1** and **2**). Note that the final reduction state in this sample is highly dominated by the Fe^{2+} state, as seen in the exemplary data in **Figure 1g**, which is likely the reason for the lack of CNT self-organization into a forest.[29] The attenuation of the Fe^0 signal as a result of decreased probed depth with increasing C 1s signal –noticeable between the magenta scan labelled 'final reduction state' and the green scan labelled 'nucleation/growth state' in **Figure 1g**– suggests that CNTs encapsulate the Fe^0 catalysts and that oxidized particles do not participate in growth. Filling of the electronic

states at the Fermi level with increase in Fe^0 content (**Figure S3**) further emphasizes the need for unbound electrons that can participate in ionic bonding during CNT growth.[46]

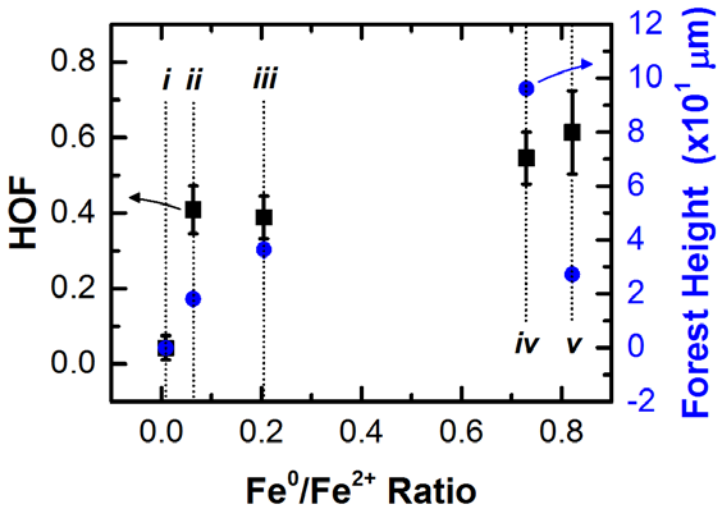

Figure 3. Forest growth metrics. Herman orientation factor, or HOF (left axis, black squares), and forest height (right axis, blue circles) as a function of Fe^0/Fe^{2+} area ratio. The HOF values show an increase in forest alignment with increase in Fe^0/Fe^{2+} ratio. Meanwhile, the forest height (obtained in a total growth time of 10 minutes) shows an increase in height with increase in Fe^0/Fe^{2+} ratio for all samples except sample **v**, which corresponded to the *in situ* deposited catalyst (see **Table 1** for sample labels). The error bars show the standard deviation in the calculated HOF and forest height values.

To test this hypothesis –that amount of fully reduced iron drives the number density of CNT-bearing catalysts– we examined sample **v**, which contained the *in situ* deposited catalyst film with a high degree of reduction prior to CNT growth (**Figure 2e** and **2j**). Although a small degree of oxidation was seen as a result of oxygen diffusion from the Al_2O_3 layer, the catalyst film in sample **v** exhibited the highest Fe^0/Fe^{2+} ratio and the cleanest surface among all the samples prior to growth. The surface cleanliness was determined by inspecting the amount of adventitious carbon prior to reduction. A high CNT density and alignment obtained from the *in situ* deposited

catalyst confirms that fully reduced iron (Fe^0) is indeed the active state of the catalyst and thus deterministic of nucleation success rate. The increase in apparent CNT density and alignment in sample **v** is consistent with results obtained for sample **iv** (**Figure 2d** and **2i**), which also exhibited a high Fe^0/Fe^{2+} ratio. In contrast, more oxidized samples with a lower Fe^0/Fe^{2+} ratio exhibited lesser alignment and CNT density, signifying a much lower nucleation success rate during growth. Our direct finding that Fe^0 is required for CNT growth is consistent with many studies that link growth to the Fe^0 state.[16-17, 32, 38, 46-48] A more reduced catalyst population gives a greater CNT nucleation density and alignment. It is important to note that other aspects of the catalyst, such as catalyst size, may influence the growth outcome. Although we did not directly examine the particle diameters as reported elsewhere,[35, 49] the CNT diameters obtained from TEM imaging (**Figure S6**) and the radial breathing modes obtained from Raman spectroscopy (**Figure S7**) indicate that neither the number of walls nor the average diameter of the CNTs was significantly impacted by the degree of reduction on these samples and that, by correspondence, neither were their precursor catalyst particles. The CNT diameters remained nearly unchanged across the samples, with a slight decrease in CNT diameter as the catalyst became more reduced. This confirms that the increase in forest density is caused by an increase in number density of CNTs and not by an increase in the CNT diameter or the number of walls. The positive correlation between the Fe^0/Fe^{2+} ratio and forest density, coupled with the unchanged CNT diameters and the attenuation of the Fe^0 signal after CNT growth, reiterate that the reduced state drives growth and that oxidized particles do not participate in the process (**Figure S8**).[46]

AP-XPS results were also used to infer growth parameters such as carbon accumulation rate (the product of growth rate and number density of nucleated catalysts) and time constant (proportional to catalyst lifetime) from the evolution of the C 1s core level spectra.[20, 26] To do so, we monitored the evolution of the C 1s area during growth, with fixed boundaries (280-295eV) and normalized to unity for consistency. The time-dependent C 1s area was fit using a linear and exponential function to extract the carbon accumulation rate and time constant, respectively. Refer to the Methods segment and supporting information (**Figures S4-S5** and comments therein)

for a detailed description on extraction of the carbon accumulation rate and time constant from AP-XPS data. An increase in accumulation rate with amount of Fe^0 (**Figure 4b**) confirms that the number of catalyst particles participating in CNT growth (and thus contributing to the C 1s signal) is proportional to the amount of catalyst that is fully reduced. Likewise, the exponential decrease in time constant with increasing Fe^0/Fe^{2+} ratio (**Figure 4c**) –although not proportional to catalyst lifetime due to limited probe depth– reiterates that the increase in carbon accumulation rate is consequential of the increase in CNT number density.

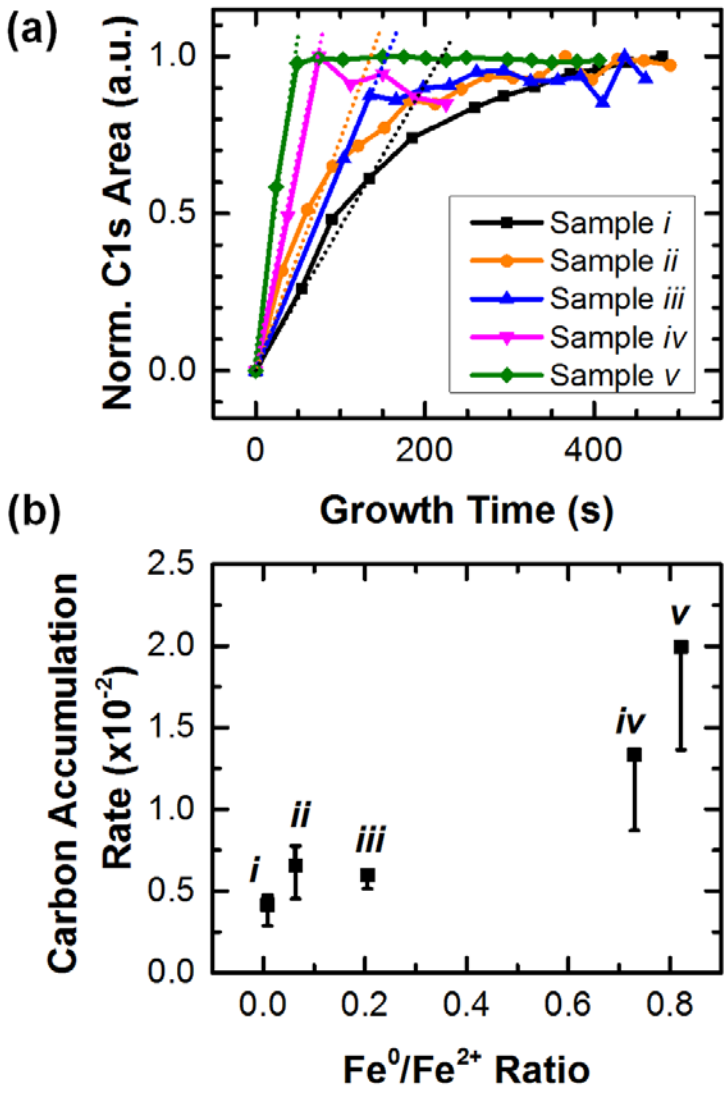

Figure 4. Carbon accumulation rate of samples in **Figure 2**. (a) Evolution of the C 1s area for samples **i-v** ranging from poor to good growth, respectively. The C 1s area was calculated with fixed boundaries and normalized to

unity for comparison, and fit with straight lines (denoted by dotted lines in panel (a)) to extract the initial growth rates. (b) The carbon accumulation rate from the fits in (a) increase with increase in Fe^0/Fe^{2+} ratio, suggesting that higher degree of catalyst reduction results in higher CNT growth rates.

Boosting Nucleation Success Rate using Carbon Preloading. In view of the importance of the population of catalyst in the fully reduced state, we now draw attention to samples **iv** and **v**, both of which have a high degree of reduction. As mentioned earlier, samples **ii-iv** (with *ex situ* deposited films) exhibit a progressive increase of hydrocarbon by-products (**Figures S9-S11**) from sequential experimentation. These samples were also exposed to oxidizing conditions prior to reduction and growth (**Figure 5**). We examined the role of these carbon by-products on catalyst reduction by monitoring the amount of carbon on the surface of the iron catalyst, expressed as the C/Fe atomic percent ratio. This ratio was obtained from the AP-XPS spectra by calculating the ratio between the area under the curve for the C 1s and Fe 2p core level spectra at the beginning of reduction, and multiplying this ratio by a factor of $2.7x10^{-2}$ to account for the difference in ionization cross-section of both core levels at the photon energy used (965eV). The calculated C/Fe ratios (black squares) are plotted against the Fe^0/Fe^{2+} ratios in **Figure 5**. Also plotted in **Figure 5** are the corresponding CNT forest heights (blue circles) obtained from **Figure 2a-e**. **Figure 5** clearly shows that the C/Fe ratio correlates with the Fe^0/Fe^{2+} ratio, and that an increase in both the C/Fe and Fe^0/Fe^{2+} ratio results in taller CNT forests. The gradual increase in C/Fe ratio is due to the progressive buildup of hydrocarbon by-products from previous growths as well as the absorption of carbon contaminants (from oxidation procedures) and water (introduced after oxidation) on the walls of the chamber and nearby components. Combined with **Figure 3**, the results show that increases in the C/Fe and Fe^0/Fe^{2+} ratios also lead to a greater CNT alignment and density.

The extent to which carbon can aid growth is demonstrated by the increase in growth ‘yield’ –the product of HOF and forest height (μm/min)– for the sample with a large quantity of carbon buildup (sample **iv**). This growth

'yield' is expressed as a product of both the HOF and forest height to account for the forest density contributing to the observed carbon accumulation rate in **Figure 4**. In comparison, the *in situ* deposited sample containing little carbon buildup and a highly reduced catalyst film (sample **v**) grew a dense forest but of shorter height. **Figures 5** and **2e** highlight how carbon can boost growth to yield forests ~3x taller than forests grown using a clean catalyst film with a comparable degree of reduction. This increase in growth yield is caused by the greater supply of carbon on preconditioned samples, which can be processed by the reduced catalyst particles at an earlier stage (**Figure S11**). Interestingly, growth of dense and highly aligned forests of comparable quality in both the *ex situ* deposited catalysts with high C/Fe ratio (sample **iv**) and the *in situ* deposited catalysts with low C/Fe ratio (sample **v**) suggests that the degree of reduction and nucleation success rate can be improved by the addition of solid carbon. This is further supported by the non-aligned growth (poor growth) obtained in the *ex situ* deposited, clean catalysts (with low C/Fe ratio, sample **i**) using identical growth conditions to those used for the *ex situ* deposited catalyst with a high C/Fe ratio (sample **iv**). Poor growth in the clean catalyst (sample **i**) as a result of minimal reduction from a highly oxidative environment and a carbon-free catalyst (**Figure 3f**) stresses the role of carbon as an additional reducing agent.[50] More importantly, we show that high density forests can be obtained by either *in situ* deposition of a highly reduced catalyst, or by reduction of an *ex situ* deposited, oxidized catalyst using a strong reducing agent. And, the *ex situ*, highly carbon-preloaded sample (sample **iv**) exhibits a greater carbon accumulation rate than the *ex situ*, clean catalyst (sample **i**) under equivalent growth conditions (**Figure 4**). While *in situ* deposition represents the ideal catalyst system (sample **v**), with the highest carbon accumulation rate among the five samples, the presence of hydrocarbons or solid carbon on the catalyst may also boost CNT growth rates and catalyst lifetime. These results suggest that CNT-bearing catalyst compete for carbon, and that exposure to excess carbon helps meet the demands for high growth rate and number density of CNTs.[51]

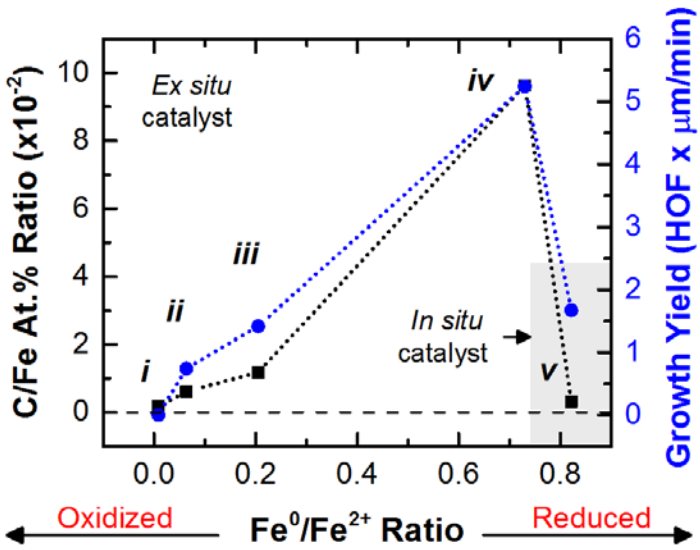

Figure 5. A highly reduced catalyst film can be obtained either by *in situ* deposition of a catalyst film in a non-oxidizing environment or by carbon-aided reduction of an *ex situ* deposited catalyst film. The C/Fe atomic percent ratio (left axis, black squares) and growth 'yield' (right axis, blue circles) for samples **i-v** show that an increase in carbon preloading can aid reduction of the catalyst and boost growth. Growth 'yield' was defined as the product of the HOF and forest height per unit time (calculated for 10 minutes of growth). The dotted lines highlight the overall dependence of growth 'yield' (right axis, blue circles) to the amount of carbon contaminants present (left axis, black squares). The black dashed line highlights the presence of minimal carbon content in sample **i** and **v**.

The improved nucleation success rate in the highly carbon-preloaded samples, containing a high C/Fe ratio, raises the question as to whether CNT-bearing particles are comprised of a carbide phase (*i.e.* Fe_3C and Fe_2O_5). This question is motivated by earlier AP-XPS studies, where nucleation of CNTs was preceded by chemisorption of carbon and formation of carbidic carbon,[13] and by *in situ* TEM work, where cementite (Fe_3C) was identified as a catalytically active phase for CNT growth.[52-54] After careful examination of the C 1s spectra taken along the reduction, nucleation, and growth stages (**Figures S10** and **S11**), we concluded that carbidic carbon was either not formed or not detected in the samples studied. This species, which is positioned at the lower-binding-energy

side of the C-C peak (~283.2 eV),[13, 55] was not detected within the time resolution of our experiments (~5-15s between sequential C 1s scans). Although the absence of this peak is not conclusive of whether a metastable carbide phase –with a life time shorter than our time resolution– was present at the onset of growth, or whether this species is quickly attenuated by the C-C peak, it is a good indicator that the boost in growth 'yield' in carbon-preloaded samples was not propelled by a carbide phase (**Figures S10** and **S11**).[13] Besides, we note that the formation of cementite is preceded by reduction of iron oxide to a fully reduced α-Fe phase (in the Fe^0 state),[46, 56] and hence the takeaway of this work remains invariant: bond formation cannot proceed unless the catalyst is in the zero-valent state, irrespective of whether it is in the form of a solid solution (*i.e.* α-Fe + carbon) or a carbide phase (Fe_3C).

Catalyst 'Readiness' is Determined by Particle Number Density in the Fe^0 state. We now refer back to the contrasting morphology of samples **i** and **iv**, which were grown using equivalent reducing and growth conditions yet exhibited significantly different degrees of catalyst reduction and CNT alignment and density. On the one hand, the growth of dense forests in sample **iv** (high Fe^0 content) resembles high-density forests obtained from catalysts supported on a strongly-interacting Al_2O_3 substrate. On the other hand, non-aligned, spaghetti-like CNT growth in sample **i** (low Fe^0 content) is morphologically similar to the poor growth obtained either from highly reduced catalysts supported on a weakly-interacting SiO_2 substrate which undergo catalyst evolution, or from catalysts supported on a strongly-interacting Al_2O_3 substrate when exposed to a low reductant or hydrocarbon pressure.[13] It is clear from the Fe^0 /Fe^{2+} ratio in **Figure 2k** that the nucleation success rate in sample **i** was limited by insufficient reduction of the catalyst as a result of its strong interaction with the Al_2O_3 support.[13, 24, 35] These two samples highlight the important role of reducing agents, experimental conditions, and catalyst-support interactions in determining the extent of reduction; the interplay between catalyst reduction and evolution may lead to a low CNT number density either due to insufficient catalyst reduction (low Fe^0/Fe^{2+} ratio) or due to particle coarsening once they are fully reduced (high Fe^0/Fe^{2+} ratio but low number density of large particles).[24,

[35, 38] Yet, the extent of reduction to the zero-valent state ultimately separates the first regime, where growth improves as Fe^0 increases, from the second regime, where growth suffers as particles coarsen.

The role of catalyst reduction on nucleation success rate during the first regime is captured in a schematic (**Figure 6**), which depicts the effects of catalyst 'readiness' on nucleation success rate. Here, we assume that only fully reduced catalyst particles can nucleate CNTs (**Figure S8**) and as such the number density of catalyst particles in the Fe^0 state determines the nucleation success rate. In the context of forest density and alignment, catalyst reduction is critical in determining the size and density of CNT-producing particles, before catalyst evolution initiates. Our results suggest that CNT self-organization, lift-off, and subsequent forest growth is achieved by increasing the number density of active particles in the Fe^0 state above the critical threshold of CNT density and alignment (~1 x 10^9 CNTs/cm^2 according to GISAXS).[27] A collective model, proposed by Bedewy *et al*., suggested five main stages of catalyst evolution and CNT-population growth dynamics: catalyst preparation, self-organization, crowding, steady growth, and termination.[27] The distributions of growth behaviors observed throughout these stages were attributed to: 1) a growth behavior dominated by the response of a small subpopulation of catalyst particles to time-invariant growth conditions suited for that subpopulation, and 2) a growth behavior dominated by the response of the remaining catalyst population to suboptimal growth conditions. Based on the present study, we propose that these stages are driven by the sub-population of catalyst particles in the Fe^0 state which are capable of CNT growth during the catalyst preparation and self-organization stages, and that the remainder of the population can be activated during the crowding stage by further reduction of the oxide film. The latter is in fact indicated by the S-shaped particle density increase ('popping') observed by Bedewy *et al*. during ETEM experiments, as will be discussed later.[27] Bedewy *et al*. also suggested that CNT-bearing particles may exhibit different evolution dynamics in comparison to those that do not bear CNTs, and that ripening may be dominated by inactive particles.[27] If this is the case, ensuring that the majority population is 'ready' (in

the active Fe^0 state) during the catalyst preparation stage can prevent particle coarsening and extend catalyst lifetime.

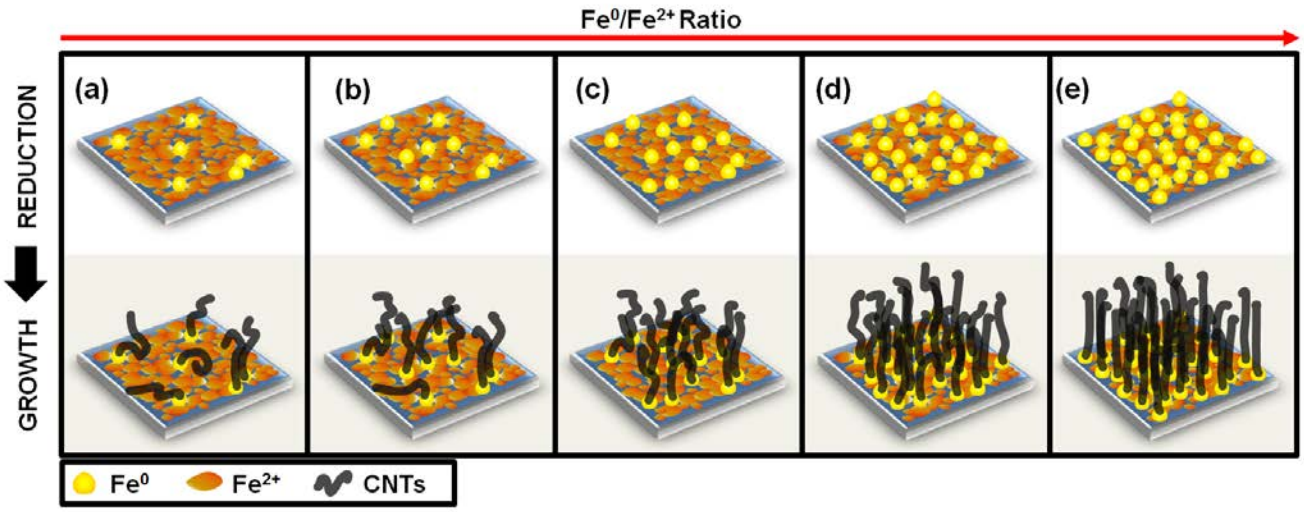

Figure 6. Schematic representation of catalyst reduction and CNT growth depicts the catalyst population density with Fe^0 and Fe^{2+} chemical states and dependence of CNT nucleation on amount of fully reduced iron (Fe^0). Nucleation success rate and alignment follows particle density in the Fe^0 state.

We reiterate that both the onset of reduction and kinetics of reduction (*i.e.* annealing time and rate) can influence the interplay between catalyst reduction and particle coarsening, and impact CNT growth.[57] These aspects of reduction have been thoroughly studied for iron films and are thus not addressed here in great detail (see supporting information for comments on the kinetics of reduction).[50, 57-60] But, we note that reduction of our iron films follows the reaction pathway reported elsewhere, Fe_2O_3 (Fe^{3+}) → Fe_3O_4 (Fe^{3+}/Fe^{2+}) → $Fe_{1-x}O$ (Fe^{2+}) → Fe (Fe^0), and that reduction to the zero-valent state in hydrogen occurs above T~430°C,[50, 57-60] as reported elsewhere and shown in **Figure 7**. The appearance of Fe^0 above this temperature indicates that the catalyst may be 'ready' (*i.e.* the catalyst is in the appropriate active state for CNT nucleation) to grow CNTs at a temperature much lower than that typically used during growth (750°C in this study),[57-58] but that the overall density of CNT-bearing nanoparticles is limited by the slow kinetics of reduction, by the use of weak reducing agents, or by catalyst-support interactions as seen elsewhere.[13, 18, 26, 38] It is clear from the pathway presented above that phase

transformation from Fe_2O_3 to Fe must be preceded by transformation to Fe_3O_4 and $Fe_{1-x}O$, and that the kinetics of these steps may retard the formation of Fe. Reduction in H_2 is slow and this critical density of fully reduced catalysts is reached only after prolonged exposure to H_2. This is the case for growth protocols that introduce H_2 concurrently with the hydrocarbon at growth temperature; therein, a decrease in number density of CNTs is presumably caused by the slow reduction kinetics of iron in an H_2 environment and by, consequentially, insufficient reduction at the point of nucleation and growth.

We thus hypothesize that during catalyst preparation in weakly reducing conditions, some of the iron atoms reduce –from the Fe^{3+} to the Fe^{2+} state and from the Fe^{2+} to the Fe^0 state– and diffuse to form particles in the Fe^0 state while the remaining iron stays in the form of an oxide (Fe^{2+} state). At the lowest reduction and dewetting temperature (above ~430°C),[27] only a few reduced particles have formed. As the temperature increases, the number density of particles in the Fe^0 state increases and after sufficient time, the critical density of reduced particles needed for CNT forest growth is reached.[60] Once the system reaches growth conditions (*i.e.* 750°C in this work), the initial density of CNTs is determined by the number density of fully reduced particles before exposure to the hydrocarbon gas. At that point, the film may be either partially reduced and composed of a mixture of Fe^{2+} bound to the support and CNT-bearing nanoparticles in the Fe^0 state, or fully reduced and composed predominantly of CNT-bearing nanoparticles in the Fe^0 state.[14] Nucleation will then take place exclusively in the particles in the active Fe^0 state. Meanwhile, reduction and particle formation from any remaining oxidized Fe is delayed; the oxidized catalyst remains inactive until fully reduced either by prolonging exposure of the catalyst to the reducing environment or by carbon-assisted reduction.[26] Under strongly reducing conditions, however, reduction takes place rapidly and prolonged exposure can result in particle coarsening, which then decreases CNT density and alignment. Particles reduced at a later stage (whether because they required more time or a stronger reducing agent) may still grow small-diameter CNTs even if particles reduced at an earlier stage became too large or can no longer produce CNTs due to other mechanisms such as poisoning. Hence, careful monitoring of the

extent of reduction (degree, onset, and kinetics) will allow optimization of nucleation success rate during growth. Our results indicate that a catalyst-support system exposed to conditions that promote rapid catalyst reduction, on the one hand, and exhibiting optimized catalyst-support interactions for impeded catalyst evolution, on the other hand, would be ideal.

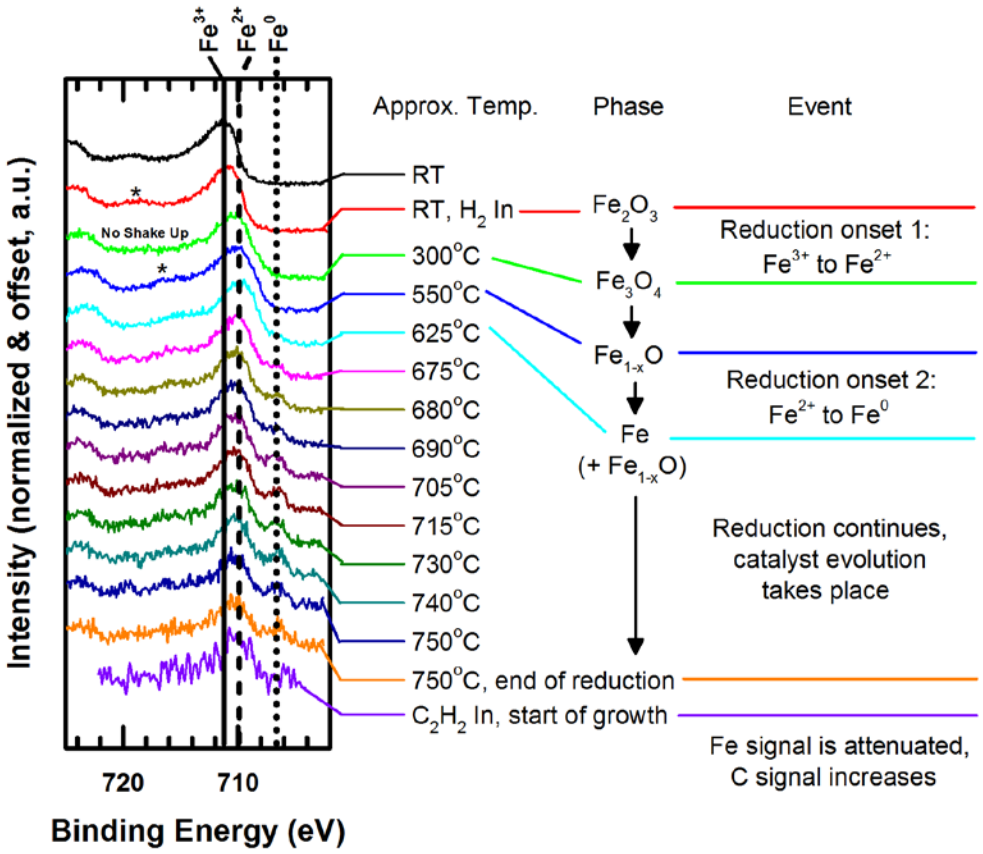

Figures 7. Kinetics of reduction of an iron catalyst film in hydrogen. AP-XPS data for sample **ii** (experimental evolution from top to bottom) confirms that reduction of our catalysts films follows the pathway reported elsewhere:[50, 57-61] Fe_2O_3 (3+)→ Fe_3O_4 (mixed 3+ and 2+)→$Fe_{1-x}O$ (2+) →Fe (0). The approximate temperature (approx. temp.), iron phases, and observable events are highlighted at various stages of the reduction process. Reduction onsets 1 and 2 denote the appearance of the Fe^{2+} and Fe^0 species, respectively. The appearance of the Fe^0 state after reduction onset 2 suggests that a small fraction of the catalyst may be able to nucleate at T>430°C,

and that catalyst evolution may begin at this point if not counterbalanced. A fraction of the film remained in the Fe^{2+} state due to the slow reduction kinetics and catalyst-support interactions.

Carbon Preloading as a Reducing Agent. We now return to the issue that the connection between CVD parameters, hidden factors such as reactor cleanliness, and CNT forest density, is not thoroughly understood. This leads to empirical practices to establish consistent growth, and limits reproducibility of results between labs and CVD systems. An increasingly common practice is the rapid heating of the catalyst in a mixture of hydrocarbon and reductant gases, resulting in smaller diameter CNTs and a higher number density of CNTs in the forest.[12] This is in contrast to CVD recipes whereby the sample is heated slowly, often in a reducing gas such as hydrogen without the hydrocarbon, which can lead to excess particle coarsening and increased particle diameters. Our AP-XPS results show that catalyst films do not reduce uniformly using reductants such as H_2 or slow annealing steps as those traditionally employed, and that reduction of the Fe catalyst can be accelerated by exposure to carbon during the annealing stage, which in turn leads to a higher nucleation density of CNTs on the substrate. The efficacy of carbon as a reducing agent is consistent with the thermodynamics of H_2 and carbon reduction in Ellingham diagrams, as well as with carbothermal reducing practices used in metallurgy.[50, 62]

We also note that "preloading" the catalyst with carbon during the nominal reduction step, here by exposure to reactor-borne contaminants from sequential experimentation without cleaning, resembles common practices in the field where a "dirty" furnace tube is relied upon to give denser and more consistent CNT forests. Herein, we noticed that sequential experimentation was promoting the accumulation of carbon by-products onto the catalyst films, and that this preloading ultimately improved the degree of reduction of the catalyst population. This is no surprise, as the role of carbon as a highly efficient reducing agent has been reported using various techniques. For instance, C_2H_2 led to improved reduction of catalysts films in AP-XPS and *in situ* XRD experiments.[12] On the other hand, *in situ* ETEM experiments showed how catalyst dewetting and particle formation is slow in a

hydrogen-only environment, and how rapid dewetting and formation of catalyst particles occurs as soon as the hydrocarbon feedstock is introduced in the ETEM chamber.[26] Likewise, GISAXS results showcased how rapid annealing in C_2H_4 can improve CNT alignment and increase the rate of self-organization up to 3-fold.[29] We believe that the previously observed S-shaped particle 'popping' and offset S-curve of CNT density reported by *in situ* TEM, and the threefold increase in organization rate reported in GISAXS experiments are governed by the reduction of the catalyst and the availability of reduced catalyst particles to nucleate CNTs when the hydrocarbon gas is introduced to the reactor. The extent to which carbon can improve nucleation probability is indicated by the use of graphene as a catalyst support, which yields forests that are twice as tall and 30% more dense.[63] Meanwhile, the spontaneous reduction of metal ions on the sidewalls of single-wall CNTs indicates that other means for reduction apart from H_2 can be used to achieve efficient electron transfer and optimize the growth process.[64]

The benefit of using controlled exposure to carbon during the reduction and dewetting stage and the generality of this approach for hot-wall CVD systems are demonstrated in a companion study by Dee *et al*., which shows a 4-fold increase in bulk mass density, an 8-fold increase in CNT number density, and a 2-fold increase in growth lifetime under otherwise identical CVD conditions. Therein, the catalyst is preload by depositing carbon onto the furnace tube prior to insertion of the catalyst.[51] The use of carbon additives in both studies, either introduced as hydrocarbon by-products from sequential experimentation, reactor preconditioning, or as solid contaminants, suggests that the catalyst preparation stage must be engineered to maximize the reduction of the catalyst, while preserving suitably sized nanoparticles. Here, for Fe films on substrates we show that a combination of heating in hydrogen and exposure to trace carbon accelerates reduction. This, in turn, gives a higher density of CNTs and implies more efficient utilization of the catalyst.

CONCLUSIONS

We have used AP-XPS to monitor catalyst 'readiness' for CNT growth, as dictated by the catalyst chemical state. We observed that CNT-bearing particles in the reduced state dictate nucleation success rate and thus influence forest density and alignment, as obtained from the Hermann orientation factor. We also revealed that poor growth is directly related to the inability to achieve a high density of catalyst particles in the reduced state prior to growth, and that a critical mass of reduced catalyst particles is required to achieve dense, tall forest growth. We observed that growth can be improved by increasing the degree of catalyst reduction (represented by the Fe^0/Fe^{2+} ratio), achieved either by depositing a reduced film or by preconditioning the catalyst film and reactor. Furthermore, we showed that carbon by-products obtained from sequential experimentation can be used as a reducing agent –superior to hydrogen– to reduce and activate more catalyst particles and increase the nucleation success rate. We propose that carbon has a dual purpose during reduction and growth: first, it may act as an electron donor to reduce catalyst films and sustain catalytic activity, and second, it may serve as a readily available carbon feedstock and participate in growth once the catalyst particles are reduced. This carbon "preloading" from sequential experimentation led to highly reduced catalyst films, which grew dense, tall forests despite the presence of oxidant (water) during growth. Highly reduced films can thus be obtained *via in situ* deposition of metallic iron, reduction of the catalyst film by selection of appropriate gas species, or by carbon preloading *via* reactor preconditioning. The results herein provide fundamental understanding of common practices used to increase nucleation success rate and provide a way forward to arrive at consistently high CNT densities by tailoring catalyst reduction kinetics.

METHODS

Sample Preparation. Silicon substrates (University wafer Si (100) substrates, 99% crystal purity, 0.5 miscut angle, *p*-type doping and 0.001-0.005 Ohm/cm resistivity) were manually cleaved to approximately 0.5 x 1cm pieces using a diamond scribe. Prior to catalyst deposition, the silicon substrates were cleaned thoroughly and coated with a 10nm film of alumina (Al_2O_3) by atomic layer deposition (ALD) at 150 ºC. The iron catalyst film

was then deposited over the alumina layer either by *ex situ* or *in situ* deposition as discussed below. For *ex situ* deposited catalyst films, the samples were transferred to an Ion Beam Sputtering/Etching System (South Bay Technology Inc., IBS/e 1511) after alumina deposition for sputtering of the iron catalyst film to a nominal thickness of 1nm. This was done by sputtering an iron target with an ionized source at 5kV accelerating voltage and 6mA emission current at a vacuum level of ~10^{-6}-10^{-7} Torr. Once the catalyst system was deposited, the samples were packaged for transportation to NSLS II. For *in situ* deposited catalyst films, the samples were packaged for transportation after deposition of the alumina film without further manipulation or deposition of a catalyst film. Once transported, the samples were introduced into the pre-loading chamber of the AP-XPS system and eventually transferred to the analysis chamber for surveying of the as-prepared surface chemical state prior to deposition. Once an initial spectral set was collected, the samples were transferred back to the pre-loading chamber which was connected to the evaporation chamber. For *in situ* deposited catalyst films, the as-cleaned supports containing 10nm of ALD alumina were pre-evacuated in the analysis chamber. Once the vacuum level was sufficiently high, the samples were transferred to the evaporation chamber. *In situ* iron deposition was carried out in the load lock chamber of the AP-XPS system which was connected to the analysis chamber *via* a gate valve. The pressure during the deposition was ~ 2x10^{-8} Torr. An SPECS EBE-4 evaporator and an iron rod (Goodfellow, 99.99% purity) were used for deposition. The deposited thickness was calibrated using a quartz crystal microbalance. Adventitious carbon in samples **ii-iv** was removed prior to reduction and growth by pre-annealing in O_2 at 400°C for 20 minutes. We note that, after cooling and removal of O_2 used for oxidation, hydrocarbon by-products were re-deposited on the sample. The source of these was, presumably, the presence of carbon by-products from previous growths on the substrate holder and heating element that were oxidized during oxidation and condensed onto the support upon cooling. **Figure S9** shows that the carbon by-products are composed of C-OH.

CNT Growth. For CNT growth the as-prepared samples were mounted in a custom-made fixture containing a heating element and introduced into the load-lock chamber of the AP-XPS system. The fixture containing the samples was loaded into the analysis chamber at a base pressure of 10^{-7}-10^{-9} Torr. The fixture position was optimized to an incidence angle of 45°. Once positioned, the samples were exposed to oxidation and reduction environments, followed by CNT growth. A semi-static fill of the desired gas was used for each experimental stage. Oxidation was conducted to remove adventitious carbon present on the surface of the samples. This was done by exposing the samples to 0.1 Torr of oxygen and heat treating them at a temperature of 400°C for 20mins. After oxidation, the samples were cooled to room temperature and the AP-XPS chamber was pumped to 10^{-2}-10^{-8} Torr. Once the desirable vacuum level was reached in the chamber, the gate valve to the turbomolecular pump was closed to allow accumulation of the residual gases in the chamber and the system base pressure was recorded before the beginning of the reducing stage. As soon as the base pressure in each experiment was established, water vapor was introduced until the desired water level was achieved. The samples were then exposed to 0.04 Torr hydrogen and heated to 750°C (~20°/min) and held for 30 minutes for catalyst reduction. Upon reaching the desired temperature, 0.1 Torr of C_2H_2 was introduced in the chamber to initiate CNT growth. After a period of 10 minutes, the C_2H_2 was removed and the samples were cooled to room temperature in the presence of hydrogen. Once cooled, the H_2 was pumped out of the chamber and the sample was exchanged. **Figures 1**, **S1**, and **S2** depict the experimental procedure and setup used. Growth conditions are listed in **Tables 1** and **S1**.

AP-XPS Data Analysis. Ambient pressure-photoelectron spectroscopy (AP-XPS) measurements were carried out at the *In situ* and *Operando* Soft X-ray Spectroscopy Beamline (IOS) in the National Synchrotron Light Source II (NSLS II). The main chamber was equipped with a differentially pumped hemispherical electron energy analyzer (Specs Phoibos 150NAP), mounted to an offset of 70° from the incident X-ray beam and 20° from the surface normal (or 110° from the surface plane). The photon energy was set to 965 eV to prevent overlap of Auger peaks with the core level spectra of interest to this study (mainly iron, carbon, oxygen and aluminum). The time

resolution, determined by the time delay between XPS scans, was ~5-30s depending on the width and conditions used for the core level of interest. CASA XPS was used for AP-XPS data analysis and peak fitting. A Shirley background was employed to analyze the Fe 2p, O 1s, C 1s and Al 2p core level spectra. Survey spectra was used to confirm that the as-prepared samples contained primarily Al, O, Fe, and C. Peak fitting was done by adjusting the number and shape of peaks depending on the core level in question. Gaussian-Lorentzian peaks of the form GL (a,n,m) were used to fit the components in the O 1s and Al 2p core level spectra. The components of the Fe $2p_{3/2}$ and $2p_{1/2}$ core level spectra were fit using a combination of asymmetric peaks (for the 3/2 and 1/2 spectra) and symmetric Gaussian-Lorentzian peaks (for their corresponding shake-up peaks) of the form LF (a,b,n,m) and GL (a,n,m), respectively. In summary, Fe 2p data was fit by 1) fitting the three main valence states (Fe^{3+}, Fe^{2+}, and Fe^{0}) at various stages of the experiments where only the pure states are present, then by 2) locking the fitting parameters, and 3) fitting the mixed valence states using the fitting parameters obtained from step 1 (*i.e.* using the Fe^{3+} and Fe^{2+} fitting parameters for Fe_3O_4). Each iron phase (Fe_2O_3, Fe_3O_4, FeO, and Fe) can also be confirmed by identifying the shake up peak in the Fe $2p_{3/2}$ spectra (asterisk in **Figures 2** and **7**). Exhaustive literature can be used as guideline for data analysis of the Fe 2p spectra.[39-44] To calculate the sensitivity factor for each elemental transition, the photoionization cross sections dependence on the photo energy was used. A quick value was obtained from this link: https://vuo.elettra.eu/services/elements/WebElements.html. Shifts resulting from sample charging and heating were corrected during data analysis by continuously monitoring the O-Al component in the Al 2p spectra and assigning this value to 74.6eV.[65] The reduction of Al and formation of metallic Fe-Al was disregarded provided that both the Al and Fe spectra shifted by the same amount.

To fit the components in the C 1s spectra, a constrained fitting procedure with a combination of symmetric peaks for the C-C (sp2) peak and symmetric Gaussian-Lorentzian peaks for all other carbon components was used.[44] To calculate the carbon accumulation rates, the C 1s evolution was monitored from time zero (t_0) before the introduction of C_2H_2 (determined as the last acquisition in the reducing step before the C_2H_2 for all samples

except sample **iii**) until the signal was saturated. This area was calculated with fixed boundaries (280-295eV) in all samples and normalized to unity for consistency. Sample **iii** required an approximation for the initial time (t_0') as detailed in the supporting information (**Figure S5**). The progression of the C 1s signal exhibited two growth behaviors in the samples: samples **i** and **ii** (with a small amount of Fe^0 signal) exhibited a self-exhausting growth behavior comprised of an initial linear growth period followed by growth decay characteristic of growth termination, whereas samples **iii**, **iv**, and **v** (with a large amount of Fe^0) exhibited a linear growth behavior followed by abrupt signal saturation. This rapid saturation was a result of faster and denser growth from a larger number density of nucleated catalysts, which rapidly extinguished the detected AP-XPS signal above the probed depth. Thus, the exponential expression used to capture the self-exhausting growth during *in situ* Raman spectroscopy work $\{A(t) = \tau * \nu \left[1 - e^{-t/\tau}\right]$, where $A(t)$ is the C 1s area, ν is the carbon accumulation rate and τ is the time constant$\}$[38] could not be used during AP-XPS analysis.[20] Instead, we extracted the carbon accumulation rate for all samples (**i-v**) by fitting a straight line to the initial portion of the growth curves (equivalent of ν in the growth expression above) and calculating the slope of the linear fit. The deviation in the carbon accumulation rates extracted from the exponential fit is shown in **Figure S5**.

Electron microscopy, Raman spectroscopy, and HOF calculations. Forest heights and CNT alignment were obtained from SEM imaging using an FEI Sirion SEM at 5kV. The Hermann Orientation Factor (HOF) values were calculated from SEM micrographs by first rotating the micrographs to align the growth axis to be vertical. Then, the FFT was extracted from each micrograph using ImageJ (thermal color insets in **Figure 2a-e**). Then, a MATLAB routine evaluated the FFT intensity as a function of the angle. Finally, the HOF was obtained by traversing around an arc in the FFT reciprocal space, with user-defined radius for the sweep. The HOF values reported are an average of 15 sweeps obtained at different radii. The associated scatter in the data is depicted as the error bar in the HOF plot. CNT diameter distributions for samples **ii-v** were obtained from TEM imaging using an FEI Titan Talos TEM at 200kV (**Figure S6**). Sample **i** could not be examined using TEM due to the low

CNT forest density. Raman scans (**Figure S7**) were obtained from the center of the CNT forest in each sample with a Renishaw Raman microscope (laser excitation 514.5 nm).

AUTHOR INFORMATION

Corresponding Author

***** E-mail: jennifer.carpena.ctr@us.af.mil

† E-mail: benjimaruyama@us.af.mil

Author Contributions

The current manuscript was written through contributions of all authors. All authors have approved submission of this manuscript.

ACKNOWLEDGEMENTS

Research carried out in part at the 23-ID-2 (IOS) beamline of the National Synchrotron Light Source-II and the Center for Functional Nanomaterials, Brookhaven National Laboratory, supported by the U.S. Department of Energy, Office of Basic Energy Sciences, Contract No. DE-SC0012704. J.Z. was supported by BNL LDRD Project No. 15-010. The authors thank Dr. A. E. Islam and Dr. P. Nikolaev for many helpful discussions. This research was performed while the author (J.C.-N.) held an NRC Research Associateship award at the Air Force Research Laboratory. The authors acknowledge support from the Air Force Office of Scientific Research under LRIR No. 16RXCOR322. N.T.D, P.R.K. and A.J.H. acknowledge support by the Department of Energy, Office of Science, Basic Energy Sciences (DE-SC0010795).

ASSOCIATED CONTENT

Supporting Information Available: Figure S1, Figure S2, Figure S3, Figure S4, Figure S5, Figure S6, Figure S7, Figure S8, Figure S9, Figure S10, Figure S11, Comments on iron reduction, Comments on the choice of experimental fit for growth rate curves, and Comments on approximating t_0' in sample **iii**. This material is available free of charge *via* the Internet at http://pubs.acs.org.

REFERENCES

1. De Volder, M. F.; Tawfick, S. H.; Baughman, R. H.; Hart, A. J. Carbon Nanotubes: Present and Future Commercial Applications. *Science* **2013**, *339*, 535-539.

2. Behabtu, N.; Young, C. C.; Tsentalovich, D. E.; Kleinerman, O.; Wang, X.; Ma, A. W.; Bengio, E. A.; ter Waarbeek, R. F.; de Jong, J. J.; Hoogerwerf, R. E.; Fairchild, S. B.; Ferguson, J. B.; Maruyama, B.; Kono, J.; Talmon, Y.; Cohen, Y.; Otto, M. J.; Pasquali, M. Strong, Light, Multifunctional Fibers of Carbon Nanotubes with Ultrahigh Conductivity. *Science* **2013**, *339*, 182-186.

3. Pengfei, Q. F., Vermesh, O., Grecu, M., Javey, A., Wang, O., Dai, H. J., Peng, S. and Cho, K. J. Toward Large Array of Multiplex Functionalized Carbon Nanotube Sensors for Highly Sensitive and Selective Molecular Detection. *Nano Lett.* **2003**, *3*, 347-351.

4. Collins, P. G.; Bradley, K.; Ishigami, M.; Zettl, A. Extreme Oxygen Sensitivity of Electronic Properties of Carbon Nanotubes. *Science* **2000**, *287*, 1801-1804.

5. Dalton, A. B.; Collins, S.; Munoz, E.; Razal, J. M.; Ebron, V. H.; Ferraris, J. P.; Coleman, J. N.; Kim, B. G.; Baughman, R. H. Super-Tough Carbon-Nanotube Fibres. *Nature* **2003**, *423*, 703.

6. Zhang, M.; Atkinson, K. R.; Baughman, R. H. Multifunctional Carbon Nanotube Yarns by Downsizing an Ancient Technology. *Science* **2004**, *306*, 1358-1361.

7. Zhang, Q.; Huang, J. Q.; Qian, W. Z.; Zhang, Y. Y.; Wei, F. The Road for Nanomaterials Industry: A Review of Carbon Nanotube Production, Post-Treatment, and Bulk Applications for Composites and Energy Storage. *Small* **2013**, *9*, 1237-1265.

8. Esconjauregui, S.; Fouquet, M.; Bayer, B. C.; Ducati, C.; Smajda, R.; Hofmann, S.; Robertson, J. Growth of Ultrahigh Density Vertically Aligned Carbon Nanotube Forests for Interconnects. *ACS Nano* **2010**, *4*, 7431-7436.

9. Futaba, D. N.; Goto, J.; Yasuda, S.; Yamada, T.; Yumura, M.; Hata, K. General Rules Governing the Highly Efficient Growth of Carbon Nanotubes. *Adv. Mater.* **2009**, *21*, 4811-4815.

10. Rao, R.; Pint, C. L.; Islam, A. E.; Weatherup, R. S.; Hofmann, S.; Meshot, E. R.; Wu, F.; Zhou, C.; Dee, N.; Amama, P. B.; Carpena-Nunez, J.; Shi, W.; Plata, D. L.; Penev, E. S.; Yakobson, B. I.; Balbuena, P. B.; Bichara, C.; Futaba, D. N.; Noda, S.; Shin, H.; *et al.* Carbon Nanotubes and Related Nanomaterials: Critical Advances and Challenges for Synthesis Toward Mainstream Commercial Applications. *ACS Nano* **2018**, *12*, 11756-11784.

11. de los Arcos, T.; Garnier, M. G.; Seo, J. W.; Oelhafen, P.; Thommen, V.; Mathys, D. The Influence of Catalyst Chemical State and Morphology on Carbon Nanotube Growth. *J. Phys. Chem. B* **2004**, *108*, 7728-7734.

12. de los Arcos, T.; Oelhafen, P.; Thommen, V.; Mathys, D. The Influence of Catalyst's Oxidation Degree on Carbon Nanotube Growth as a Substrate-Independent Parameter. *J. Phys. Chem. C* **2007**, *111*, 16392-16396.

13. Hofmann, S.; Sharma, R.; Ducati, C.; Du, G.; Mattevi, C.; Cepek, C.; Cantoro, M.; Pisana, S.; Parvez, A.; Cervantes-Sodi, F.; Ferrari, A. C.; Dunin-Borkowski, R.; Lizzit, S.; Petaccia, L.; Goldoni, A.; Robertson, J. *In Situ* Observations of Catalyst Dynamics During Surface-Bound Carbon Nanotube Nucleation. *Nano Lett.* **2007**, *7*, 602-608.

14. Mattevi, C.; Wirth, C. T.; Hofmann, S.; Blume, R.; Cantoro, M.; Ducati, C.; Cepek, C.; Knop-Gericke, A.; Milne, S.; Castellarin-Cudia, C.; Dolafi, S.; Goldoni, A.; Schloegl, R.; Robertson, J. *In-Situ* X-Ray Photoelectron Spectroscopy Study of Catalyst−Support Interactions and Growth of Carbon Nanotube Forests. *J. Phys. Chem. C* **2008**, *112*, 12207-12213.

15. Mattevi, C.; Hofmann, S.; Cantoro, M.; Ferrari, A. C.; Robertson, J.; Castellarin-Cudia, C.; Dolafi, S.; Goldoni, A.; Cepek, C. Surface-Bound Chemical Vapour Deposition of Carbon Nanotubes: *In Situ* Study of Catalyst Activation. *Phys. E (Amsterdam, Neth.)* **2008**, *40*, 2238-2242.

16. Hofmann, S.; Blume, R.; Wirth, C. T.; Cantoro, M.; Sharma, R.; Ducati, C.; Havecker, M.; Zafeiratos, S.; Schnoerch, P.; Oestereich, A.; Teschner, D.; Albrecht, M.; Knop-Gericke, A.; Schlogl, R.; Robertson, J. State of Transition Metal Catalysts during Carbon Nanotube Growth. *J. Phys. Chem. C* **2009**, *113*, 1648-1656.

17. Wirth, C. T.; Hofmann, S.; Robertson, J. State of the Catalyst During Carbon Nanotube Growth. *Diamond Relat. Mater.* **2009**, *18*, 940-945.

18. Esconjauregui, S.; Fouquet, M.; Bayer, B. C.; Eslava, S.; Khachadorian, S.; Hofmann, S.; Robertson, J. Manipulation of the Catalyst-Support Interactions for Inducing Nanotube Forest Growth. *J. Appl. Phys.* **2011**, *109*, 044303.

19. Nishimura, K.; Okasaki, N.; Pan, L.; Nakayama, Y. *In Situ* Study of Iron Catalysts for Carbon Nanotube Growth Using X-Ray Diffraction Analysis. *Jpn. J. Appl. Phys.* **2004**, *43*, L 471–L 474.

20. Rao, R.; Liptak, D.; Cherukuri, T.; Yakobson, B. I.; Maruyama, B. *In Situ* Evidence for Chirality-Dependent Growth Rates of Individual Carbon Nanotubes. *Nat. Mater.* **2012**, *11*, 213-216.

21. Rao, R.; Pierce, N.; Liptak, D.; Hooper, D.; Sargent, G.; Semiatin, S. L.; Curtarolo, S.; Harutyunyan, A. R.; Maruyama, B. Revealing the Impact of Catalyst Phase Transition on Carbon Nanotube Growth by *In Situ* Raman Spectroscopy. *ACS Nano* **2013**, *7*, 1100-1107.

22. Nikolaev, P.; Hooper, D.; Perea-Lopez, N.; Terrones, M.; Maruyama, B. Discovery of Wall-Selective Carbon Nanotube Growth Conditions *via* Automated Experimentation. *ACS Nano* **2014**, *8*, 10214-10222.

23. Rao, R.; Sharma, R.; Abild-Pedersen, F.; Norskov, J. K.; Harutyunyan, A. R. Insights into Carbon Nanotube Nucleation: Cap Formation Governed by Catalyst Interfacial Step Flow. *Sci. Rep.* **2014**, *4*, 6510 (6).

24. Kim, S. M.; Pint, C., L. ; Amama, P. B.; Hauge, R. H.; Maruyama, B.; Stach, E. A. Catalyst and Catalyst Support Morphology Evolution in Single-Walled Carbon Nanotube Supergrowth: Growth Deceleration and Termination. *J. Mater. Res.* **2010**, *25*, 1875-1885.

25. Balakrishnan, V.; Bedewy, M.; Meshot, E. R.; Pattinson, S. W.; Polsen, E. S.; Laye, F.; Zakharov, D. N.; Stach, E. A.; Hart, A. J. Real-Time Imaging of Self-Organization and Mechanical Competition in Carbon Nanotube Forest Growth. *ACS Nano* **2016**, *10*, 11496-11504.

26. Bedewy, M.; Viswanath, B.; Meshot, E. R.; Zakharov, D. N.; Stach, E. A.; Hart, A. J. Measurement of the Dewetting, Nucleation, and Deactivation Kinetics of Carbon Nanotube Population Growth by Environmental Ttransmission Electron Microscopy. *Chem. Mater.* **2016**, *28*, 3804-3813.

27. Bedewy, M.; Meshot, E. R.; Reinker, M. J.; Hart, A. J. Population Growth Dynamics of Carbon Nanotubes. *ACS Nano* **2011**, *5*, 8974-8989.

28. Landois, P.; Pinault, M.; Rouziere, S.; Porterat, D.; Mocuta, C.; Elkaim, E.; Mayne-L'Hermite, M.; Launois, P. *In Situ* Time Resolved Wide Angle X-Ray Diffraction Study of Nanotube Carpet Growth: Nature of Catalyst Particles and Progressive Nanotube Alignment. *Carbon* **2014**, *87*, 246-256.

29. Meshot, E. R.; Verploegen, E.; Bedewy, M.; Tawfick, S.; Woll, A. R.; Green, K. S.; Hromalik, M.; Koerner, L. J.; Philipp, H. T.; Tate, M. W.; Gruner, S. M.; Hart, A. J. High-Speed *In Situ* X-Ray Scattering of Carbon Nanotube Film Nucleation and Self-Organization. *ACS Nano* **2012**, *6*, 5091-5101.

30. Meshot, E. R.; Zwissler, D. W.; Bui, N.; Kuykendall, T. R.; Wang, C.; Hexemer, A.; Wu, K. J. J.; Fornasiero, F. Quantifying the Hierarchical Order in Self-Aligned Carbon Nanotubes from Atomic to Micrometer Scale. *ACS Nano* **2017**, *11*, 5405-5416.

31. Hofmann, S.; Cantoro, M.; Kleinsorge, B.; Casiraghi, C.; Parvez, A.; Robertson, J.; Ducati, C. Effects of Catalyst Film Thickness on Plasma-Enhanced Carbon Nanotube Growth. *J. Appl. Phys.* **2005**, *98*, 034308.

32. Nessim, G. D.; Hart, A. J.; Kim, J. S.; Acquaviva, D.; Oh, J.; Morgan, C. D.; Seita, M.; Leib, J. S.; Thompson, C. V. Tuning of Vertically-Aligned Carbon Nanotube Diameter and Areal Density through Catalyst Pre-Treatment. *Nano. Lett.* **2008,** *8*, 3587-3593.

33. Nessim, G. D.; Seita, M.; O'Brien, K. P.; Hart, A. J.; Bonaparte, R. K.; Mitchell, R. R.; Thompson, C. V. Low Temperature Synthesis of Vertically Aligned Carbon Nanotubes with Electrical Contact to Metallic Substrates Enabled by Thermal Decomposition of the Carbon Feedstock. *Nano Lett.* **2009**, *9*, 3398-3405.

34. Amama, P. B.; Zemlyanov, D.; Sundarakannan, B.; Katiyar, R. S.; Fisher, T. S. XPS and Raman Characterization of Single-Walled Carbon Nanotubes Grown from Pretreated Fe_2O_3 Nanoparticles. *J. Phys. D: Appl. Phys.* **2008**, *41*, 165306.

35. Amama, P. B.; Pint, C. L.; Kim, S. M.; McJilton, L.; Eyink, K. G.; Stach, E. A.; Hauge, R. H.; Maruyama, B. Influence of Alumina Type on the Evolution and Activity of Alumina-Supported Fe Catalysts in Single-Walled Carbon Nanotube Carpet Growth. *ACS Nano* **2010**, *4*, 895-904.

36. Yamada, T.; Maigne, A.; Yudasaka, M.; Mizuno, K.; Futaba, D. N.; Yumura, M.; Lijima, S.; Hata, K. Revealing the Secret of Water-Assisted Carbon Nanotube Synthesis by Microscopic Observation of the Interaction of Water on the Catalysts. *Nano Lett.* **2008**, *8*, 4288-4292.

37. Zhang, G.; Mann, D.; Zhang, L.; Javey, A.; Li, Y.; Yenilmez, E.; Wang, Q.; McVittie, J. P.; Nishi, Y.; Gibbons, J. Ultra-High-Yield Growth of Vertical Single-Walled Carbon Nanotubes: Hidden Roles of Hydrogen and Oxygen. *Proc. Natl. Acad. Sci. U. S. A.* **2005**, *102*, 16141-16145.

38. Shi, W.; Li, J.; Polsen, E. S.; Oliver, C. R.; Zhao, Y.; Meshot, E. R.; Barclay, M.; Fairbrother, D. H.; Hart, A. J.; Plata, D. L. Oxygen-Promoted Catalyst Sintering Influences Number Density, Alignment, and Wall Number of Vertically Aligned Carbon Nanotubes. *Nanoscale* **2017**, *9*, 5222-5233.

39. McIntyre, N. S.; Zetaruk, D. G. X-Ray Photoelectron Spectroscopic Studies of Iron Oxides. *Anal. Chem.* **2002**, *49*, 1521-1529.

40. Graat, P.; Somers, M. A. J. Quantitative Analysis of Overlapping XPS Peaks by Spectrum Reconstruction: Determination of the Thickness and Composition of Thin Iron Oxide Films. *Surf. Interface Anal.* **1998**, *26*, 773-782.

41. Graat, P. C. J.; Somers, M. A. J. Simultaneous Determination of Composition and Thickness of Thin Iron-Oxide Films from XPS Fe 2p Spectra. *Appl. Surf. Sci.* **1996**, *100/101*, 36-40.

42. Fujii, T.; de Groot, F. M. F.; Sawatzky, G. A.; Voogt, F. C.; Hibma, T.; Okada, K. *In Situ* XPS Analysis of Various Iron Oxide Films Grown by NO_2-Assisted Molecular-Beam Epitaxy. *PRB* **1999**, *59*, 3195-3202.

43. Coreille, J. S.; He, J.-W.; Goodman, D. W. Preparation and Characterization of Ultra-Thin Iron Oxide Films on a Mo (100) Surface. *Surf. Sci.* **1995**, *338*, 211-224.

44. Bhargava, G.; Gouzman, I.; Chun, C. M.; Ramanarayanan, T. A.; Bernasek, S. L. Characterization of the "Native" Surface Thin Film on Pure Polycrystalline Iron: A High Resolution XPS and TEM study. *Appl. Surf. Sci.* **2007**, *253*, 4322-4329.

45. Lin, H.-Y.; Chen, Y.-W.; Li, C. The Mechanism of Reduction of Iron Cxide by Hydrogen. *Thermochim. Acta* **2003**, *400*, 61-67.

46. Plata, D. L.; Meshot, E. R.; Reddy, C. M.; Hart, A. J.; Gschwend, P. M. Multiple Alkynes React with Ethylene to Enhance Carbon Nanotube Synthesis, Suggesting a Polymerization-Like Formation Mechanism. *ACS Nano* **2010**, *4*, 7185-7192.

47. Plata, D. L.; Hart, A. J.; Reddy, C. M.; Gschwend, P. M. Early Evaluation of Potential Environmental Impacts of Carbon Nanotube Synthesis by Chemical Vapor Deposition. *Environ. Sci. Technol.* **2009**, *43*, 8367-8373.

48. Meshot, E. R.; Plata, D. L.; Tawfick, S.; Zhang, Y.; Verploegen, E. A.; Hart, A. J. Engineering Vertically Aligned Carbon Nanotube Growth by Decoupled Thermal Treatment of Precursor and Catalyst. *ACS Nano* **2009**, *3*, 2477-2486.

49. Chen, G.; Seki, Y.; Kimura, H.; Sakurai, S.; Yumura, M.; Hata, K.; Futaba, D. N. Diameter Control of Single-Walled Carbon Nanotube Forests from 1.3-3.0 nm by Arc Plasma Deposition. *Sci. Rep.* **2014**, *4*, 3804 (7).

50. Cyprès, R.; Soudan-Moinet, C. Pyrolysis of Coal and Iron Oxides Mixtures. 2. Reduction of Iron Oxides. *Fuel* **1981**, *60*, 33-39.

51. Dee, N. T.; Li, J.; Orbaek White, A.; Jacob, C.; Shi, W.; Kidambi, P. R.; Cui, K.; Zakharov, D. N.; Janković, N. Z.; Bedewy, M.; Carpena-Núñez, J.; Maruyama, B.; Stach, E. A.; Plata, D. L.; Hart, A. J. Carbon-Assisted Catalyst Pretreatment Enables Straightforward Synthesis of High-Density Carbon Nanotube Forests. Carbon, in review.

52. Yoshida, H.; Takeda, S.; Uchiyama, T.; Kohno, H.; Homma, Y. Atomic-Scale *In-Situ* Observation of Carbon Nanotube Growth from Solid State Iron Carbide Nanoparticles. *Nano Lett.* **2008**, *8*, 2082-2086.

53. Sharma, R.; Moore, E.; Rez, P.; Treacy, M. M. Site-Specific Fabrication of Fe Particles for Carbon Nanotube Growth. *Nano Lett.* **2009**, *9*, 689-694.

54. Mazzucco, S.; Wang, Y.; Tanase, M.; Picher, M.; Li, K.; Wu, Z.; Irle, S.; Sharma, R. Direct Evidence of Active and Inactive Phases of Fe Catalyst Nanoparticles for Carbon Nanotube Formation. *J. Catal.* **2014**, *319*, 54-60.

55. Wiltner, A.; Linsmeier, C. Formation of Endothermic Carbides on Iron and Nickel. *Phys. Status Solidi A* **2004**, *201*, 881-887.

56. Perez-Cabero, M.; Taboada, J. B.; Guerrero-Ruiz, A.; Overweg, A. R.; Rodriguez-Ramos, I. The Role of Alpha-Iron and Cementite Phases in the Growing Mechanism of Carbon Nanotubes: a 57Fe Mossbauer Spectroscopy Study. *Phys. Chem. Chem. Phys.* **2006**, *8*, 1230-1235.

57. Munteanu, G.; Ilieva, L.; Andreeva, D. Kinetic Parameters Obtained from TPR Data for α-Fe_2O_3 and Systems. *Thermochim. Acta* **1997**, *291*, 171-177.

58. Lin, H.-Y.; Chen, Y.-W.; Li, C. The Mechanism of Reduction of Iron Oxide by Hydrogen. *Thermochim. Acta* **2003**, *400*, 61-67.

59. Jozwiak, W. K.; Kaczmarek, E.; Maniecki, T. P.; Ignaczak, W.; Maniukiewicz, W. Reduction Behavior of Iron Oxides in Hydrogen and Carbon Monoxide Atmospheres. *Appl. Catal., A* **2007**, *326*, 17-27.

60. Abd Rashid, R. Z.; Mohd. Salleh, H.; Ani, M. H.; Yunus, N. A.; Akiyama, T.; Purwanto, H. Reduction of Low Grade Iron Ore Pellet Using Palm Kernel Shell. *Renewable Energy* **2014**, *63*, 617-623.

61. Oh, J.; Noh, D. The Reduction Kinetics of Hematite Particles in H_2 and CO Atmospheres. *Fuel* **2017**, *196*, 144-153.

62. Hayward, C. R. Extraction of Metals from Ores. *J. Chem. Educ.* **1943**, *20*, 29-32.

63. Rao, R.; Pierce, N.; Harutyunyan, A. R. Enhancement of Vertically Aligned Carbon Nanotube Growth Kinetics and Doubling of the Height by Graphene Interface. *J. Phys. Chem. C* **2014**, *118*, 22243-22248.

64. Choi, H. C.; Shim, M.; Bangsaruntip, S.; Dai, H. Spontaneous Reduction of Metal Ions on the Sidewalls of Carbon Nanotubes. *J. Am. Chem. Soc.* **2002**, *124*, 9058-9059.

65. van den Brand, J.; Sloof, W. G.; Terryn, H.; de Wit, J. H. W. Correlation between Hydroxyl Fraction and O/Al Atomic Ratio as Determined from XPS Spectra of Aluminum Oxide Layers. *Surf. Interface Anal.* **2004**, *36*, 81-88.